



Nanocalorimetry using microscopic optical wireless integrated circuits

Conrad L. Smart^a, Alejandro J. Cortese^a, B. J. Ramshaw^{a,b}, and Paul L. McEuen^{a,b,1}

Contributed by Paul L. McEuen; received March 26, 2022; accepted October 7, 2022; reviewed by Chris Dames and Eric Pop

We present in situ calorimetry, thermal conductivity, and thermal diffusivity measurements of materials using temperature-sensing optical wireless integrated circuits (OWiCs). These microscopic and untethered optical sensors eliminate input wires and reduce parasitic effects. Each OWiC has a mass of ~100 ng, a 100-μm-scale footprint, and a thermal response time of microseconds. We demonstrate that they can measure the thermal properties of nearly any material, from aerogels to metals, on samples as small as 100 ng and over thermal diffusivities covering four orders of magnitude. They also function over a broad temperature range, and we present proof-of-concept measurements of the thermodynamic phase transitions in both liquid crystal 5CB and gadolinium.

calorimetry | microscopic | sensor

The thermal properties of materials are of major fundamental and practical interest, critical for understanding everything from phase transitions in high-temperature superconductors (1) to the dynamics of protein folding (2, 3) to heat dissipation in ntegrated circuits (4, 5). However, it is often difficult to measure these properties, particularly in small samples with fast thermal response times. Contact techniques (6) use resistors and thermocouples for heating and sensing (7-9) that are easy to use but add to the thermal mass and contribute to parasitic heat loss. Miniaturization of thermistors like in scanning thermal microscopy (SThM) (10) offer nanoscale temperature resolution at the cost of scan speed while also requiring complex instrumentation. Noncontact optical methods (11) such as infrared thermometry (12), laser-flash methods (13), Raman spectroscopy (14), and thermoreflectance (15-17) avoid these issues and offer nanoscale spatial resolution but require advanced optical expertise and extra cleanroom fabrication steps (15). The lack of a simple, noninvasive, and general purpose, approach to thermal measurements, on small samples in particular, is a major impediment to everything from combinatoric materials discovery (18) to real-time, in situ monitoring of microscale systems.

Here, we demonstrate that optical wireless integrated circuits (OWiCs) (19) can solve this problem. By combining the electronic thermometry of contact techniques with the optical I/O of noncontact approaches, we create a fast, reliable thermal measurement device in a package only 100 µm on a side. To demonstrate its capabilities, we measure heat capacities of samples as small as 100 ng, thermal diffusivities of materials ranging over 4 orders of magnitude, and the signatures of structural and magnetic phase transitions, all with microsecond response times. The combination of speed, range, and ease of use make thermal OWiCs a valuable tool for materials discovery, thermal characterization, and temperature monitoring.

Results and Discussion

An OWiC (Fig. 1A) consists of an array of silicon photovoltaics (PVs) in series with an AlGaAs/GaAs light-emitting diode (LED) in an integrated microscopic package $8 \mu m \times 75 \mu m \times 175 \mu m$ and weighing only 100 ng. Fig. 1B shows the all-optical I/O of the OWiC with the photovoltaics and LED harvesting and emitting light, respectively. OWiCs are fabricated in parallel on a silicon-on-insulator (SOI) wafer and can be released by dry etching the underlying silicon substrate [see Cortese et al. (19) for details]. Aluminum release tags tether the OWiC to the substrate and can be broken away and placed on a sample by micromanipulators or micropipettes as shown in Fig. 1 C. For smooth surfaces and liquids, the OWiC typically makes good thermal contact to the sample. For rough surfaces, a small amount of thermal paste (Apiezon vacuum grease) is used. A schematic of the optical microscope for powering and measuring the OWiC is depicted in *SI Appendix*, Fig. S1.

Significance

One of the key aspects of materials discovery is understanding the way heat moves through a material, with applications across the scientific spectrum from superconducting phase transitions to binding mechanisms in amino acids. However, the smaller the sample under study (e.g., small crystals of quantum materials), the more difficult it becomes to measure heat flow with standard macroscopic calorimeters. Here, we show that we can use optical wireless integrated circuits (OWiCs) as microscopic calorimeters for noninvasive, in situ, measurements of the thermal conductivity, diffusivity, and heat capacity of almost any material, from aerogel to silicon, on samples down to 100 ng, including across phase transitions. The OWiCs are an all-purpose thermal measurement tool that can transform the way scientists explore and discover new materials.

Author contributions: C.L.S., A.J.C., B.J.R., and P.L.M. designed research; C.L.S. performed research; C.L.S., A.J.C., and B.J.R. contributed new reagents/analytic tools; C.L.S., A.J.C., and P.L.M. analyzed data; and C.L.S., B.J.R., and P.L.M. wrote the paper.

Reviewers: C.D., University of California Berkeley; and E.P., Stanford University.

Competing interest statement: A.J.C. and P.L.M. are both founders of OWiC Technologies, a startup that has licensed from Cornell the optical wireless integrated circuit technology used in this paper.

Copyright © 2022 the Author(s). Published by PNAS. This article is distributed under Creative Commons Attribution-NonCommercial-NoDerivatives License 4.0 (CC BY-NC-ND).

¹To whom correspondence may be addressed. Email: plm23@cornell.edu.

This article contains supporting information online at http://www.pnas.org/lookup/suppl/doi:10.1073/pnas. 2205322119/-/DCSupplemental.

Published November 3, 2022.

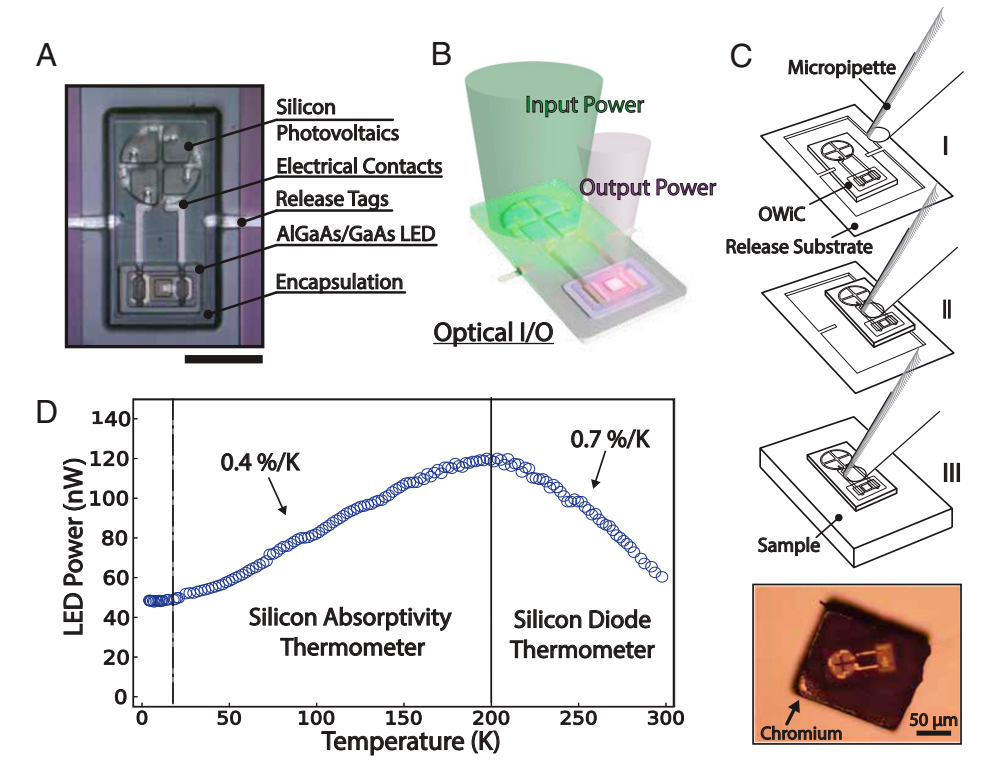


Fig. 1. OWIC thermometer. (A) Microscope image of the OWIC as fabricated on SOI chip before release. (Scale bar: 50 μm.) (B) Optical I/O of the OWIC. The OWiC is powered by illumination of the on-board photovoltaics and transmits temperature information via the optical output intensity of the on-board LED. (C) Schematic of pick-and-place method using micropipette to (I) break away the release tags, (II) move the OWiC off the release substrate, (III) place the OWiC directly onto samples. For example, the Bottommost image in (C) shows the OWiC placed directly on a 200 µm x 200 µm x 10 µm chromium chip. (D) Thermometer behavior of the OWiC from 4 K to 300 K.

When the PVs are illuminated with light intensities $> 1 \mu W/\mu m^2$, the on-board LED emits infrared light (840 nm) whose intensity is proportional to the temperature T over broad ranges (Fig. 1D). This behavior is due to two well-known mechanisms. Above 200 K, the open-circuit voltage of the silicon photovoltaics decreases with T at the ratio of the bandgap energy of silicon to the Boltzmann constant, $E_g/k_B \cong 2 \text{ mV/K}$ per photovoltaic (20), leading to a decreasing output light. This saturates when the LED becomes current-limited around 200 K; below this the temperature dependence of the silicon absorptivity dominates. Silicon is an indirect bandgap material and optical absorption involves the absorption/emission of phonons, leading to a temperature dependence that is reasonably approximated as linear in temperature (21). A full analysis of the circuit model can be found in SI Appendix, Fig. S2. The light output thus serves as a local thermometer with a sensitivity on the order of 1%/K. The measurement noise is approximately 10^{-4} K/ $\sqrt{\text{Hz}}$, set primarily by optical shot noise (SI Appendix, Fig. S1).

We first use the OWiC to measure the heat capacity of small samples. An OWiC on microgram-mass silicon chip approximately 250 μ m \times 180 μ m \times 10 μ m in size is shown in Fig. 2A and a cross-section of the experiment geometry is shown in Fig. 2A, Inset. The sample sits on thin oxide posts 4 µm in diameter and 10 µm long that thermally isolate it from the substrate. The posts are photolithographically patterned and etched with inductively coupled plasma reactive ion etching (ICP RIE); fabrication details along with analysis of the thermal model can be found in SI Appendix, Figs. S8 and S9.

Under illumination, the temperature of the silicon sample (and attached OWiC) rises and reaches a steady state. This is shown in Fig. 2B for three different heating powers. The initial heating rate $\delta T/\delta t$, the steady-state temperature change ΔT ,

and the heating time (tens of milliseconds) are easily resolved by the OWiC.

The thermal properties can be extracted by using Newton's law of heating:

$$\Delta T(t) = \frac{\dot{Q}}{G_{ox}} (1 - e^{-t/\tau}), \qquad [1]$$

where Q is the heating power estimated from the absorptivity of the silicon photovoltaics (22), $G_{ox} = k_{ox} A_{post} / L_{post}$ is the thermal conductance of the oxide posts, and $\tau = (C_{sample} +$ $C_{OWiC})/G_{ox}$ is the thermal relaxation time of the OWiCsample-post system; the ratio of the sample and OWiC heat capacities to the thermal conductance. The heat loss mechanism is dominated by the conductance through the oxide posts; the contributions from radiative and convective heat loss are discussed in the SI Appendix. The OWiC heating traces and model fits are shown in Fig. 2B. The fits match the data extremely well, yielding the heat capacity of the sample $C = 2 \mu J/K$. The thermal conductance of the posts is found to be $G_{ox} = 0.5 \text{ mW/K}$, yielding a thermal conductivity of the posts $k_{ox} = 1.4 \text{ Wm}^{-1} \text{ K}^{-1}$, consistent with values $(1.2-1.5 \text{ Wm}^{-1} \text{ K}^{-1})$ reported in the literature (23).

The heat capacity scales with the sample mass. Fig. 2C shows the heating trace from a 3.5 µg silicon sample, 1 µg silicon sample, and the standalone OWiC (~100 ng). Fig. 2D shows the measured heat capacity for a variety of silicon and chromium samples with masses ranging from 1 µg to 9 µg. The heat capacity scales linearly with sample mass for both materials. The slope corresponds to the specific heat c = C/M of the material, the heat capacity C normalized by the mass M. We measure the specific heat of silicon $c_{si} = 0.41 \pm 0.05 \text{ J g}^{-1} K^{-1}$

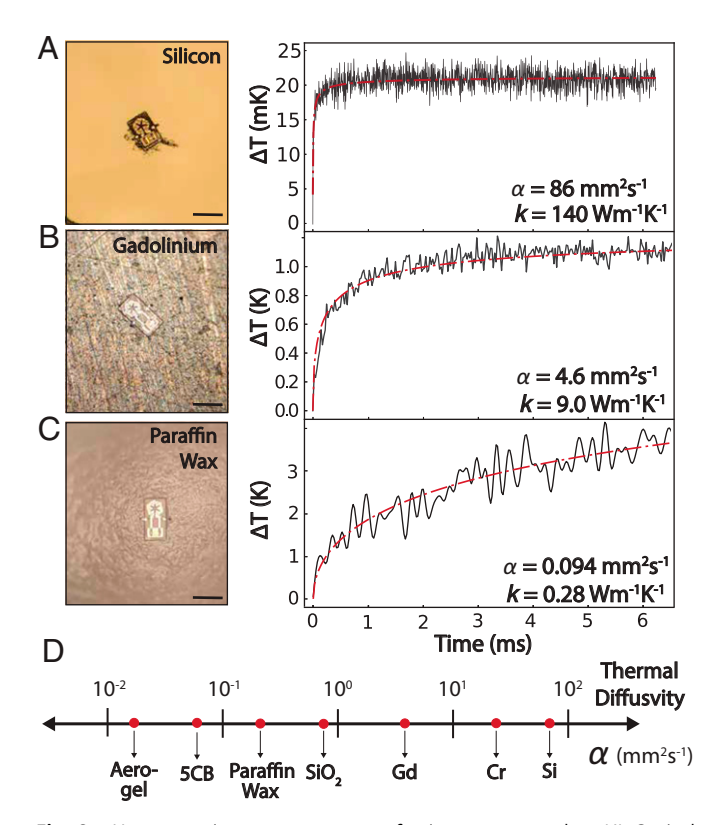


Fig. 2. Heat capacity measurements of microgram samples. (A) Optical microscope image of the OWiC on a small silicon chip on silicon dioxide posts. (Scale bar: 100 µm.) (B) Example heating traces (black) as measured from the OWiC on a microgram sample under different optical heating powers fit with Eq. 1 (red, dashed). (C) Example heating traces (black) as measured by the OWiC for silicon samples with different masses, as well as the standalone OWiC, fit with Eq. 1 (red). (D) The measured heat capacity for different sample masses of silicon (blue), chromium (red), and the standalone OWiC (star). The OWiC heat capacity was measured to be ~100 nJ/K.

and chromium $c_{Cr} = 0.72 \pm 0.05 \text{ J g}^{-1} K^{-1}$. Both measured values are in good agreement with the previously reported values of 0.45 $\rm Jg^{-1}~K^{-1}$ (24) and 0.70 $\rm Jg^{-1}~K^{-1}$ (25).

The heat capacity of the standalone OWiC is measured to be $C_{OWiC} \approx 100$ nJ/K at room temperature. This is shown in Fig. 2E as a star in the bottom left corner. This value corresponds to the thermal addenda contribution from the OWiC; a miniscule value compared to standard heat capacity measurement systems [e.g., Quantum Design PPMS, ~15 mJ/K at 400 K (9)]. The OWiC heat capacity determines the smallest sample we can easily measure through the requirement $C_{sample} > C_{OWiC}$. This corresponds to masses >100 ng for materials with typical specific heats.

The above results demonstrate that OWiCs can measure the heat capacity of samples down to a few hundred nanograms. We now show that they can also quickly and quantitatively measure both the thermal diffusivity α_s and thermal conductivity k_s (as well as the heat capacity $c_s = k_s/\rho\alpha_s$) of almost any material, without any special preparation. The only requirement is that the sample be a few times larger than the OWiC in all dimensions, corresponding to \sim 0.5 mm on a side.

Fig. 3 A–C shows example measurements. The OWiC is placed directly onto a variety of materials and a small amount of interstitial thermal paste is used between the OWiC and the surface to ensure good thermal contact. The measurements were performed in a vacuum at $\sim 10^{-4}$ atm. Upon illumination, the laser heats the sample locally. The OWiC's temperature rises rapidly, then begins to level off and eventually reaches a maximum temperature at long time scales. The amount and rate of heating, which depends on the material's thermal conductivity and thermal diffusivity, varies by orders of magnitude for the three materials shown in Fig. 3 A-C.

To extract the thermal coefficients, we model the OWiC as a half-sphere heat source of effective radius R_{eff} and the material as a semi-infinite solid (26) a method closely related to the

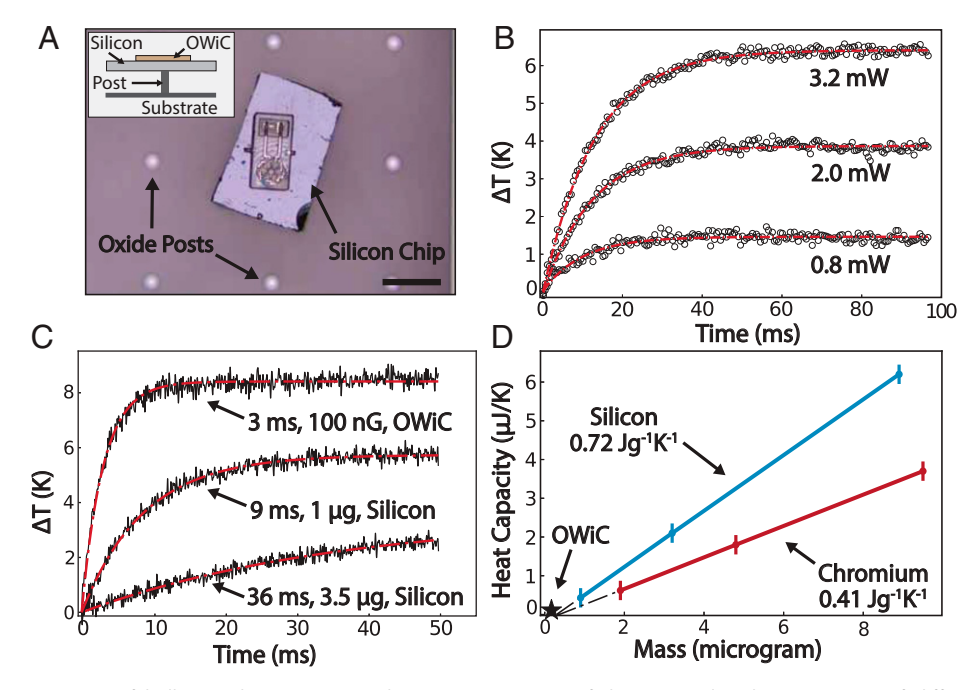


Fig. 3. Thermal characterization of bulk samples. (A-C) Optical microscope image of the OWiC placed on a variety of different materials (Left) and the corresponding heating trace associated with the material (Right). The heating data (black) is fit with Eq. 2 (red) which is used to extract the thermal diffusivity and thermal conductivity of the substrate. Different heating powers were used for the samples: 100 mW for silicon, 4.3 mW for Gd, 0.9 mW for liquid crystal. (D) Range of materials measured with the OWiC with thermal diffusivities spanning four orders of magnitude from silica aerogel to silicon. (Scale bars: ~100 um.)

transient "hot-disk" method (27). The change in temperature as a function of time is:

$$\Delta T(t) = \frac{\dot{Q}}{2\pi R_{eff} k_s} \left(1 - \exp\left(\frac{\alpha_s t}{R_{eff}^2}\right) \operatorname{erfc}\left(\frac{\sqrt{\alpha t}}{R_{eff}}\right) \right), \quad [2]$$

where \dot{Q} is the heating power from the input laser, k_s and α_s are the thermal conductivity and thermal diffusivity of the sample, respectively. The radius R_{eff} depends on the specific geometry of the OWiC, and we experimentally determine it by measuring a reference material of known thermal properties, a 4-inch, polished silicon wafer (25). We find $R_{eff} = 40 \ \mu \text{m} \pm 1 \ \mu \text{m}$.

Fits of Eq. 2 to the heating traces of three samples are shown in Fig. 3 A–C. The fits closely match the measured data. From the fit, we extract both the thermal diffusivity and specific heat of the sample material. For example, using the data in Fig. 3B, we measure the thermal diffusivity of gadolinium (Gd) to be $\alpha_s = 4.3 \pm 0.4$ mm²/s. This is within the uncertainty of the previously measured value of 4.4 mm²/s (28).

Using this technique, we measured the thermal properties of a very broad range of materials, as depicted in Fig. 3D (full traces for each sample can be found in SI Appendix, Figs. S5 and S6 along with a discussion about the sensitivity of the fits in SI Appendix, Fig. S7). Table 1 lists the measured properties along with previously reported values for each material. In general, we find very good agreement. This four-orders-of-magnitude range in diffusivity encompasses a wide selection of materials, from aerogels (29) to ordered single crystals (25). OWiCs are thus a broadly useful tool for probing the thermal properties of almost any solid or liquid.

As a final demonstration of the utility of OWiCs, we measure the specific heat and diffusivity of materials near a phase transition. Studies of phase transitions are one of the most important applications of thermal measurements, revealing, for example, the order of the phase transition, the latent heat, etc. However, they can be difficult to probe, since the behavior occurs over a narrow temperature range and sometimes produces only small changes in the thermal properties. We show that OWiCs have the necessary resolution, examining both a first order transition, the nematic—isotropic transition in the liquid crystal (LC) 5CB, and a second order one, the ferromagnet—paramagnet transition in Gd.

We choose the nematic-isotropic phase transition of LC 5CB as a first test for two reasons: it has a large heat capacity signature at the transition (33), and the birefringence of the LC in nematic phase (long-range orientational order and no

translational order) allows easy visualization of the ordering of the molecules using polarization microscopy.

A droplet of 5CB was deposited on a silicon substrate using a small diameter micropipette. The OWiC was placed directly on top of the droplet. Fig. 4A shows several temperature points crossing the nematic-isotropic transition ($T_c = 308 \text{ K}$). At 307 K (I) the color bands indicate long-range nematic order across the entire droplet. From 308 K (II) to 309 K (III) the color bands become more local, until at 310 K (IV) they disappear entirely when the 5CB reaches a fully isotropic state.

Fig. 4B shows the measured thermal diffusivity, thermal conductivity, and specific heat for the temperature range of 295–318 K. A minimum is visible in the diffusivity and maximum in the specific heat near 308 K. The thermal conductivity shows a step near this same temperature. The four red dashes near the transition temperature in each plot refer to the corresponding polarization microscope images (I–IV) in Fig. 4A. To extract quantitative values, we treated the LC as a block of material immediately underneath the footprint of the OWiC (Fig. 4 B, Inset) with a much lower thermal conductivity and diffusivity than the OWiC and silicon. We then used Newton's law of heating (Eq. 1); details are found in the SI Appendix.

These features and width of the transition are qualitatively and quantitatively consistent with previously reported results (33). The magnitude of the diffusivity change and the stepwise function in the conductivity (from lower to higher) are in accordance with a planar LC 5CB alignment relative to the substrate in the nematic phase, likely caused by trapping the liquid crystal between the silicon substrate and OWiC.

We now turn to the magnetic phase transition in Gd. An OWiC was placed directly on top of a piece of Gd foil 500 µm thick (Sigma Aldrich, 99.9% purity) as shown in Fig. 4C. Heating traces were compiled for a range of temperatures from 270 K to 310 K, and the data were analyzed using the semi-infinite model (Eq. 2). Fig. 4D shows the measured thermal diffusivity, thermal conductivity, and specific heat of Gd across the temperature range of 270–310 K. The thermal diffusivity decreases with increasing temperature until 290 K, then shows a step up around 295 K before continuing to rise. The measured heat capacity shows a distinct maximum around 290 K. The thermal conductivity remains mostly constant throughout the measured range, although with a slight increase near the higher temperatures.

These features are qualitatively and quantitatively consistent with previous measurements (Fig. 4, black) of the ferromagnetic-paramagnetic phase transition in Gd (28, 35, 37), again demonstrating the ability of a 100 μ m-sized OWiC to reproduce the results obtained using larger, more complex apparatus.

Table 1. List of materials measured using the OWiC

	Thermal diffusivity (mm ² /s)		Thermal conductivity (Wm ⁻¹ K ⁻¹)		Specific heat (Jg ⁻¹ K ⁻¹)	
Material*	Previous work	This work	Previous work	This work	Previous work	Inferred
Aerogel (1 atm) (29, 30)	0.06-0.1	0.054(0.006)	0.015-0.03	0.0152(0.0003)	1.5-5.0	2.8(0.3)
Paraffin wax (31, 32)	0.08-0.2	0.098(0.006)	0.15-0.35	0.277(0.002)	2.1-3.0	2.8(0.2)
LC 5CB (33)	0.06-0.12	0.13(0.02)	0.12-0.24	0.24(0.01)	1–2	1.9(0.3)
Silicon dioxide (23, 34)	0.83	0.87(0.09)	1.2-1.5	1.17(0.03)	0.71	0.59(0.06)
Gd (28, 35)	4.4	4.3(0.4)	8–10	9.2(0.3)	0.22-0.35	0.27(0.03)
Chromium (24, 36)	30	29(3)	93	79(5)	0.45	0.38(0.04)
Silicon (25)	88	85(9)	140 [†]		0.7	0.71(0.07)

The measured thermal diffusivity, thermal conductivity, and specific heat was measured for each material and compared to published values. The reported silicon thermal conductivity value was used as a reference material and has been grayed out in the table.

^{*}All values given at room temperature and 10⁻⁴ atm unless denoted otherwise.

 $^{^{\}dagger}$ Reference material for inferring the effective radius, R_{eff}

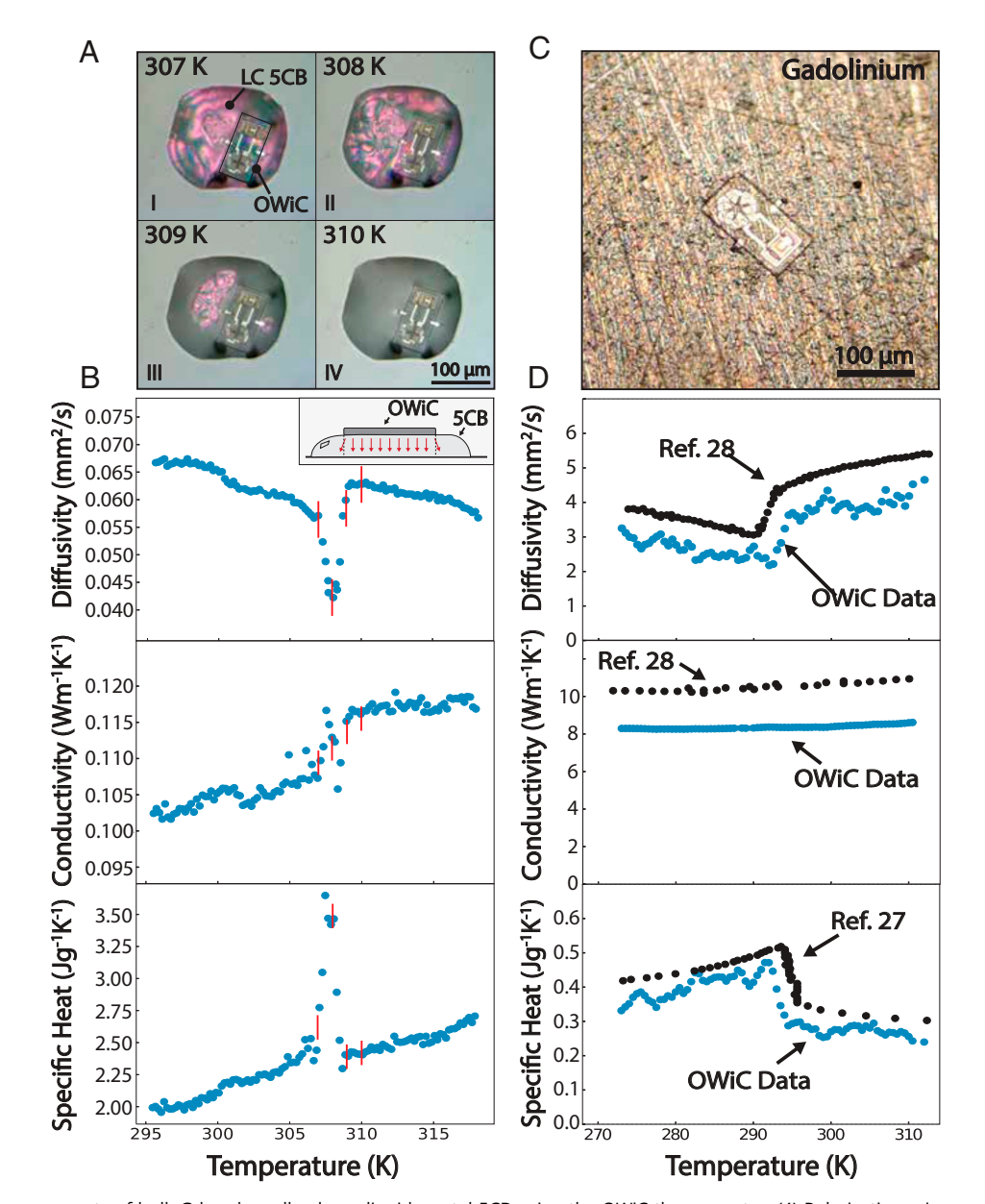


Fig. 4. Thermal measurements of bulk Gd and small volume liquid crystal 5CB using the OWiC thermometer. (A) Polarization microscopy of the OWiC in a small droplet of liquid crystal 5CB for four different temperatures. The birefringent property of 5CB in a nematic state is visible as light and dark bands depending on the local ordering of the molecules. The ordering disappears as the LC transitions from a nematic state (<308 K) to a liquid state (>308 K). (B) Thermal diffusivity, thermal conductivity, and specific heat of the small droplet of 5CB from 295 K to 318 K as measured by the OWiC (blue). The four red marks refer to the corresponding image in (A) Inset: schematic of the OWiC on a platform of liquid crystal. (C) Optical image of the OWiC on a piece of rough Gd. (D) In descending order, thermal diffusivity, thermal conductivity, and specific heat of the Gd from 270 K to 310 K as measured by the OWiC (blue) and compared to previous work (black).

The results presented here show the utility and versatility of the OWiC thermal sensors, combining the best features of contact and noncontact thermometry. OWiCs have the potential to dramatically change how thermal measurements are performed in the future. They are accurate, fast, and can be placed in a wide variety of environments for in situ or in vivo thermal characterization. They can accurately measure the heat capacity of samples down to 100 ng in mass, and quantitatively measure specific heat and diffusivity of nearly any material (including through phase transitions) all with a temperature resolution of 10^{-4} K/ $\sqrt{}$ Hz. Future designs will integrate complementary metal-oxide-semiconductor circuitry to reduce the power consumption and explore intensity independent measurement schemes. Potential applications include everything from rapid probing the heat capacity of microcrystals too small for traditional

methods (38) to local thermal measurements of biological tissue in vivo (39).

Materials and Methods

An upright microscope (BX51WI, Olympus) was modified for simultaneous optical microscopy, laser heating, and optical recording. In imaging mode, a halogen lamp (TH4-100, Olympus) is used as a light source, and the image is collected in a CCD camera. To heat the OWiC a continuous wave laser (MGL-III-532-200mW, Ready Laser) is modulated with a digital acousto-optical modulator (AOMO 3080-125, Gooch and Housego) and reflected off a dichroic mirror (805 nm cut-on, DMLP805R, Thorlabs) into the back aperture of a 20× Olympus microscope objective (PLN 20x, Olympus). The laser incident onto the OWiC illuminates the on-board silicon photovoltaics. We treat the incident light as uniform across the diameter of the beam. The output light of the OWiC from the AlGaAs/GaAs LED is collected by the objective, focused onto an avalanche silicon

photodetector (APD410A, Thorlabs) and sent to a digital oscilloscope (PS5000, Picoscope). Detailed *Materials and Methods* can be found in the *SI Appendix*.

Data, Materials, and Software Availability. All study data are included in the article and/or SI Appendix.

ACKNOWLEDGMENTS. This work was performed in part at the Cornell Nano-Scale Facility, an National Nanotechnology Coordinated Infrastructure (NNCI)

- J. Zhang et al., Anomalous thermal diffusivity in underdoped YBa2Cu3O6+x. Proc. Natl. Acad. Sci. U.S.A. 114, 5378-5383 (2017).
- S. Wang et al., Micro-differential scanning calorimeter for liquid biological samples. Rev. Sci. Instrum. 87, 105005 (2016).
- L. J. J. Laarhoven, P. Mulder, D. D. M. Wayner, Determination of bond dissociation enthalpies in solution by photoacoustic calorimetry. Acc. Chem. Res. 32, 342-349 (1999).
- E. Pop, Energy dissipation and transport in nanoscale devices. Nano Res. 3, 147-169 (2010).
- H. Tang et al., Review of applications and developments of ultra-thin micro heat pipes for electronic cooling. Appl. Energy 223, 383-400 (2018).
- E. Gmelin, Classical temperature-modulated calorimetry: A review. Thermochim. Acta 304-305,
- R. Bachmann et al., Heat capacity measurements on small samples at low temperatures. Rev. Sci. Instrum. 43, 205-214 (1972).
- D. W. Denlinger et al., Thin film microcalorimeter for heat capacity measurements from 1.5 to 800 K. Rev. Sci. Instrum. 65, 946-959 (1994).
- J. C. Lashley et al., Critical examination of heat capacity measurements made on a Quantum Design physical property measurement system. Cryogenics 43, 369-378 (2003).
- S. Deshmukh et al., Direct measurement of nanoscale filamentary hot spots in resistive memory devices. Sci. Adv. 8, eabk1514 (2022).
- B. Abad, D.-A. Borca-Tasciuc, M. S. Martin-Gonzalez, Non-contact methods for thermal properties measurement. Renew. Sustain. Energy Rev. 76, 1348-1370 (2017).
- D. Teyssieux, L. Thiery, B. Cretin, Near-infrared thermography using a charge-coupled device camera: Application to microsystems. Rev. Sci. Instrum. 78, 034902 (2007).
- K. Shinzato, T. Baba, A laser flash apparatus for thermal diffusivity and specific heat capacity measurements. J. Therm. Anal. Calorim. 64, 413-422 (2001).
- M. Kuball et al., Time-resolved temperature measurement of AlGaN/GaN electronic devices using micro-raman spectroscopy. IEEE Electron Device Lett. 28, 86-89 (2007).
- E. P. Visser, E. H. Versteegen, W. J. P. van Enckevort, Measurement of thermal diffusion in thin films using a modulated laser technique: Application to chemical-vapor-deposited diamond films. J. Appl. Phys. 71, 3238-3248 (1992).
- 16. G. L. Eesley, Generation of nonequilibrium electron and lattice temperatures in copper by picosecond laser pulses. Phys. Rev. B Condens. Matter 33, 2144-2151 (1986).
- A. J. Schmidt, R. Cheaito, M. Chiesa, A frequency-domain thermoreflectance method for the characterization of thermal properties. Rev. Sci. Instrum. 80, 094901 (2009)
- P. J. McCluskey, J. J. Vlassak, Combinatorial nanocalorimetry. J. Mater. Res. 25, 2086-2100 (2010).
- A. J. Cortese et al., Microscopic sensors using optical wireless integrated circuits. Proc. Natl. Acad. Sci. U.S.A. 117, 9173-9179 (2020).
- P. Löper et al., Analysis of the temperature dependence of the open-circuit voltage. Energy Procedia 27, 135-142 (2012).
- J. Noffsinger, E. Kioupakis, C. G. Van de Walle, S. G. Louie, M. L. Cohen, Phonon-assisted optical absorption in silicon from first principles. Phys. Rev. Lett. 108, 167402 (2012).

member supported by the NSF (NNCI-2025233), and the Cornell Center for Materials Research Shared Facilities which are supported through the NSF MRSE program (DMR-1719875).

Author affiliations: ^aLaboratory of Atomic and Solid-State Physics, Cornell University, Ithaca, NY 14853; and ^bKavli Institute at Cornell for Nanoscale Science, Cornell University, Ithaca, NY 14853

- 22. M. A. Green, Self-consistent optical parameters of intrinsic silicon at 300K including temperature coefficients. Sol. Energy Mater. Sol. Cells 92, 1305-1310 (2008).
- E. H. Ratcliffe, Thermal conductivities of fused and crystalline quartz. Br. J. Appl. Phys. 10, 22-25 (1959)
- E. Fawcett, Spin-density-wave antiferromagnetism in chromium. Rev. Mod. Phys. 60, 209-283
- Touloukian, Y. S. Powell, R. W. Ho, C. Y, and Klemens, P. G, Thermal Conductivity-Metallic Elements and Alloys, Purdue University, Lafeyette, IN (United States), 1970. 1.
- H. S. Carslaw, J. C. Jaeger, J. Jaeger John Conrad, Conduction of Heat in Solids (Clarendon Press,
- 27. M. Gustavsson, E. Karawacki, S. E. Gustafsson, Thermal conductivity, thermal diffusivity, and specific heat of thin samples from transient measurements with hot disk sensors. Rev. Sci. Instrum. **65**, 3856-3859 (1994).
- 28. M. Griffel, R. E. Skochdopole, F. H. Spedding, The Heat Capacity of Gadolinium from 15 to 355°K. Phys. Rev. 93, 657-661 (1954).
- O. Nilsson, Å. Fransson, O. Sandberg, "Thermal properties of silica aerogel in aerogels" in Springer Proceedings in Physics, J. Fricke, Ed. (Springer, 1986), pp. 121-126.
- Q. Liu et al., Flexible transparent aerogels as window retrofitting films and optical elements with tunable birefringence. Nano Energy 48, 266-274 (2018).
- P. Zbińkowski, J. Zmywaczyk, P. Koniorczyk, Experimental investigations of thermophysical properties of some paraffin waxes industrially manufactured in Poland. AIP Conf. Proc. 1866, 040044 (2017).
- 32. N. Ukrainczyk, S. Kurajica, J. Šipušić, Thermophysical comparison of five commercial paraffin waxes as latent heat storage materials. Chem. Biochem. Eng. Q. 24, 129-137 (2010).
- M. Marinelli, F. Mercuri, U. Zammit, F. Scudieri, Thermal conductivity and thermal diffusivity of the cyanobiphenyl (nCB) homologous series. Phys. Rev. E Stat. Phys. Plasmas Fluids Relat. Interdiscip. Topics 58, 5860-5866 (1998).
- 34. H. Kanamori, H. Mizutani, N. Fujii, Method of thermal diffusivity measurement. J. Phys. Earth 17, 43-53 (1969).
- C. Glorieux, J. Thoen, Thermal and magnetic properties of gadolinium by acoustic detection of optically and magnetically induced temperature oscillations. J. Phys. IV France 04, C7-C274
- J. P.Moore, R. K.Williams, R. S. Graves, Thermal conductivity, electrical resistivity, and Seebeck coefficient of high-purity chromium from 280 to 1000 K. J. Appl. Phys. 48, 610-617
- 37. K. A. Gschneidner, Metals, alloys and compounds-highpurities do make a difference! J. Alloys Compd. 193, 1-6 (1993).
- T. Ishibe et al., Heat transport through propagon-phonon interaction in epitaxial amorphouscrystalline multilayers. Commun. Phys. 4, 1-7 (2021).
- R. C. Webb et al., Ultrathin conformal devices for precise and continuous thermal characterization of human skin. Nat. Mater. 12, 938-944 (2013).